Four-α-Helix Bundle with Designed Anesthetic Binding Pockets. Part II: Halothane Effects on Structure and Dynamics

Tanxing Cui,* Vasyl Bondarenko,* Dejian Ma,* Christian Canlas,* Nicole R. Brandon,* Jonas S. Johansson,[§¶] Yan Xu,*[†] and Pei Tang*[†‡]

*Department of Anesthesiology, [†]Department of Pharmacology, and [‡]Department of Computational Biology, University of Pittsburgh School of Medicine, Pittsburgh, Pennsylvania 15260; [§]Department of Anesthesiology and Critical Care, and [¶]Johnson Research Foundation, Department of Biochemistry and Biophysics, University of Pennsylvania, Philadelphia, Pennsylvania 19104

ABSTRACT As a model of the protein targets for volatile anesthetics, the dimeric four-α-helix bundle, (Aα_2-L1M/L38M)$_2$, was designed to contain a long hydrophobic core, enclosed by four amphipathic α-helices, for specific anesthetic binding. The structural and dynamical analyses of (Aα_2-L1M/L38M)$_2$ in the absence of anesthetics (another study) showed a highly dynamic antiparallel dimer with an asymmetric arrangement of the four helices and a lateral accessing pathway from the aqueous phase to the hydrophobic core. In this study, we determined the high-resolution NMR structure of (Aα_2-L1M/L38M)$_2$ in the presence of halothane, a clinically used volatile anesthetic. The high-solution NMR structure, with a backbone root mean-square deviation of 1.72 Å (2JST), and the NMR binding measurements revealed that the primary halothane binding site is located between two side-chains of W15 from each monomer, different from the initially designed anesthetic binding sites. Hydrophobic interactions with residues A44 and L18 also contribute to stabilizing the bound halothane. Whereas halothane produces minor changes in the monomer structure, the quaternary arrangement of the dimer is shifted by about half a helical turn and twists relative to each other, which leads to the closure of the lateral access pathway to the hydrophobic core. Quantitative dynamics analyses, including Modelfree analysis of the relaxation data and the Carr-Purcell-Meiboom-Gill transverse relaxation dispersion measurements, suggest that the most profound anesthetic effect is the suppression of the conformational exchange both near and remote from the binding site. Our results revealed a novel mechanism of an induced fit between anesthetic molecule and its protein target, with the direct consequence of protein dynamics changing on a global rather than a local scale. This mechanism may be universal to anesthetic action on neuronal proteins.

INTRODUCTION

A diverse range of molecules, from structurally featureless noble gases to complex steroids, can render people into a state of mind commonly known as general anesthesia. The molecular processes underlying this phenomenon remain unclear (1–7). Although modulation of neuronal protein functions through nonspecific anesthetic perturbation to the lipids in the central nervous system remains a distinct possibility, the current consensus is that anesthetic molecules, despite their structural diversity, interact specifically with proteins (5). Extensive investigations, particularly with biophysics, electrophysiology, and mutagenesis approaches, have centered on the hypothesis that anesthetics occupy the hydrophobic pockets or cavities in the proteins to change the protein function. How exactly such a change is achieved, however, is still a mystery.

The dimeric protein, (Aα_2-L1M/L38M)$_2$, was engineered by de novo design to create a long hydrophobic core within a common four-α-helix bundle scaffold (8,9). This four-α-helix bundle has an anesthetic binding affinity in the anesthetizing concentration range of clinical volatile anesthetics (9,10) and thus is regarded as a suitable model for the protein targets of general anesthetics. In our Part I article in this issue (11), we presented the NMR structural and dynamical analysis of (Aα_2-L1M/L38M)$_2$ in the absence of anesthetic binding. The apoprotein backbone structure was resolved to a root mean-square deviation (RMSD) of 1.77 Å. As originally designed, two monomers of the helix-turn-helix motif form an antiparallel dimer. The dimeric structure shows that two helices from the N-terminus to the linker (helix 1 and helix 1′) are held together by the ring stacking of F12 and W15 along the hydrophobic core and by a leucine zipper from complementary pairs of L4, L11, L18, and L25 at the heptad *e* position of each monomer. The high-resolution structure also shows a lateral access pathway near K47 between the two second helices in the dimer (helix 2 and helix 2′) such that the amphipathic anesthetic molecules can enter the hydrophobic core directly from the aqueous phase. Departing from the initial design, however, is the number of anesthetic binding pockets identifiable within the hydrophobic core. Whereas the original design intended to create two sites with mirror images of each other between W15 and M38 of each monomer (9), the NMR structure suggests only one primary anesthetic binding site between the aromatic rings of W15 in the dimer, and two possible minor binding sites between the ring stacking of F12 and F52 (11).

In this study, we experimentally measured the halothane binding to (Aα_2-L1M/L38M)$_2$ and determined the

Submitted July 19, 2007, and accepted for publication January 18, 2008.

Address reprint requests to Professor Pei Tang or Professor Yan Xu, 2049 Biomedical Science Tower 3, 3501 Fifth Avenue, Pittsburgh, PA 15260. Tel.: 412-383-9798; Fax: 412-648-8998; E-mail: tangp@anes.upmc.edu or xuy@anes.upmc.edu.

Editor: Susan P. Gilbert.

0006-3495/08/06/4464/09 $2.00

doi: 10.1529/biophysj.107.117853

high-resolution structure of $(A\alpha_2\text{-L1M/L38M})_2$ in the presence of halothane. Comparison of the structures and dynamics of $(A\alpha_2\text{-L1M/L38M})_2$ in the presence and absence of a bound halothane molecule revealed an interesting change in protein quaternary structure and in the overall dynamics of the protein. These results shed new light on how volatile anesthetics might potentially produce functional changes in proteins in general.

MATERIALS AND METHODS

$(A\alpha_2\text{-L1M/L38M})_2$ expression and purification, NMR sample preparation, and all NMR methods for structure determination have been described in detail in Part I (11). Briefly, the conventional suite of two-dimensional (2D) and three-dimensional (3D) heteronuclear, filtered experiments for spectral assignment, TALOS dihedral angle constraints, and NOESY distance constraints were carried out using the standard pulse sequences from the Bruker sequence library. ^{15}N- and ^{13}C-filtered NOESY was measured with a mixing time of 120 ms. The NOESY assignment was done initially using the Cyana program (12) and then improved manually. Because of the high helical content in $(A\alpha_2\text{-L1M/L38M})_2$ and the characteristic short- and mid-range NOE connectivity to define the helix regions in the structure, the long-range intersubunit NOEs from residues on the opposite ends of the helices can be distinctively and positively identified by the chemical shift matching with an exclusion strategy, without resorting to mixing labeled and unlabeled samples and using specific filtering or purging pulse sequences. In the halothane titration experiments, the $(A\alpha_2\text{-L1M/L38M})_2$ concentration was 500 μM in 10%D_2O/90%H_2O with 0.4% 2,2-dimethyl-2-silapentane-5-sulfonic acid (DSS) and 0.02% NaN_3. Neat halothane was added in 0.3 μl increments using a Hamilton microsyringe. Because evaporation during the repeated titration procedure could not be controlled, the halothane concentrations in the NMR sample were measured by the halothane ^{1}H intensities after each titration step and then calibrated against the final titration point, at which both ^{1}H and ^{19}F intensities were measured, with the ^{19}F intensity calibrated against known concentrations of trifluoroacetate solutions (13,14). Based on this calibration, the halothane concentrations in the titration experiment ranged from 0 to 2.2 mM, at which point the chemical shift change started to plateau. At very low halothane concentrations, the halothane peak was too weak to be accurately measured. This technical difficulty prevents the site-specific K_d values from being accurately quantified. Therefore, the chemical shift change as a function of halothane titration is used in this study only as a qualitative indication of the halothane binding site(s). To estimate the magnitude of K_d at the binding site, nonlinear regression with the following equation (15,16) was used to fit the chemical shift changes as a function of halothane concentration, including the point with zero halothane:

$$\Delta_{obs} = \frac{\Delta_{max}}{2[P]_0}\left\{\left(K_D + [A]_0 + [P]_0\right) - \sqrt{\left(K_D + [A]_0 + [P]_0\right)^2 - 4[A]_0[P]_0}\right\}, \quad (1)$$

where $[A]_0$ and $[P]_0$ are the anesthetic and protein concentration, respectively, and Δ_{max} is the limiting chemical shift difference.

Except for temperature dependent amide proton exchange measurements, for which HSQC experiments were performed at 25, 30, 35, and 40°C to determine the temperature coefficient for hydrogen bonding constraints, all other NMR experiments were conducted at 35°C. Most of the NMR experiments were carried out using a Bruker Avance 600 spectrometer. For selected experiments, Avance 700 and 800 spectrometers were used.

Two different types of experiments were conducted to determine the halothane binding to $(A\alpha_2\text{-L1M/L38M})_2$ by measuring the intermolecular NOE. The conventional 2D ^{1}H-^{1}H NOESY was used to measure the coherent NOE build-up, whereas selective saturation transfer was used to measure the noncoherent cross relaxation between the two interacting molecules. The ^{1}H saturation transfer NOE experiments used tr-HSQC-based pulse sequence. Selective saturation of halothane proton resonance was achieved using an IBURP2 pulse train (80-ms shaped pulses with an interpulse delay of 4 μs and a total duration of 1.6 s) preceding the tr-HSQC sequence. Interleaving on-resonance and off-resonance (–5000 Hz) spectra were acquired to determine the saturation-transfer effects between halothane and individual residues.

The halothane effects on backbone dynamics were measured in the presence of 2.2 mM halothane and compared with the results obtained without halothane as described in Part 1 (11). The ^{15}N R_1 and R_2 relaxation and ^{15}N-{^{1}H} heteronuclear NOE (hetNOE) data were analyzed using the Lipari-Szabo model-free approach (17,18) with the Modelfree program (19).

The R_2 relaxation dispersion spectra were acquired at 35°C on Bruker 800 MHz NMR spectrometers with ^{15}N operating frequencies of 81.09 MHz. The spectra were recorded with 1024 t_2 and 128 t_1 data points, with spectral widths of 10 ppm for ^{1}H and 24 ppm for ^{15}N dimensions. The relaxation-compensated constant-time Carr-Purcell-Meiboom-Gill (CPMG) sequence was used (20,21). The total CPMG constant-time delay was set to T_{CPMG} = 60 ms (two 30 ms CPMG periods). The spectra were collected with 10 different CPMG field strengths, measured by ν_{CPMG} of 33.33, 66.67, 100.00, 133.33, 200.00, 266.67, 333.33, 400.00, 500.00, and 666.67 Hz, where $\nu_{CPMG} = 1/(4\tau_{CPMG})$, and the separation between the centers of successive refocusing 180° pulses equals $2\tau_{CPMG}$. An additional reference spectrum was collected by removing the CPMG periods in the pulse sequence. A relaxation delay of 2.5 s was used. The ^{1}H chemical shifts were referenced to DSS resonance at 0 ppm, and the ^{15}N chemical shifts were indirectly referenced (22).

To analyze transverse relaxation dispersion, the intensities of crosspeaks in 2D R_2 relaxation dispersion spectra with a given CPMG field strength were measured and then converted into the ^{15}N transverse relaxation rate constant R_2 and associated uncertainties according to the well-established relations (23):

$$R_2(\nu_{CPMG}) = -\frac{1}{T_{CPMG}}\ln\left(\frac{I(\nu_{CPMG})}{I_0}\right) \quad (2)$$

and

$$dR_2(\nu_{CPMG}) = \frac{1}{T_{CPMG}}\left[\left(\frac{dI(\nu_{CPMG})^2}{I(\nu_{CPMG})^2}\right) + \left(\frac{dI_0^2}{I_0^2}\right)\right]^{1/2}, \quad (3)$$

where $I(\nu_{CPMG})$ and I_0 are the intensities for a given crosspeak, and $dI(\nu_{CPMG})$ and dI_0 are the noise levels in the dispersion spectra with and without the CPMG pulse trains, respectively. Three exchange parameters, R_{20}, Φ_{ex}/k_{ex} and k_{ex} were calculated using the fast exchange limit approximation ($\Delta\omega = \omega_a - \omega_b < k_{ex}$) with two exchanging sites to fit the R_2 dispersion profile $R_2(\nu_{CPMG})$ by (24):

$$R_2(\nu_{CPMG}) = R_{20} + \frac{\Phi_{ex}}{k_{ex}}\left(1 - \frac{4\nu_{CPMG}}{k_{ex}}\tanh\left(\frac{k_{ex}}{4\nu_{CPMG}}\right)\right), \quad (4)$$

in which R_{20} is the R_2 without exchange (in the limit of $\nu_{CPMG} = \infty$), $\Phi_{ex} = (\omega_a - \omega_b)^2 p_a p_b$, p_i and ω_i are the populations and Larmor frequencies for the nuclear spin in site i; and k_{ex} is the exchange rate. It should be noted that k_{ex} describes exchange rate on the μs-ms timescale and is not the same as the phenomenological R_{ex} term used in the Modelfree approach (24,25).

RESULTS

Site-specific anesthetic binding

Two independent NMR methods were used to determine possible site-specific interactions between anesthetics and $(A\alpha_2\text{-L1M/L38M})_2$. The first was an anesthetic titration ex-

periment, in which the dependence of chemical shifts of individual residues in $(A\alpha_2\text{-L1M/L38M})_2$ was measured as a function of halothane concentration. Fig. 1 *A* depicts the representative overlaps of HSQC contour plots for four residues where the backbone amide ^1H or ^{15}N chemical shifts are profoundly affected by varying concentration of halothane. Nonlinear fitting with Eq. 1, including the point without halothane, yield an estimate of K_d at W15 to be 2.6 ± 1.7 mM ($R^2 = 0.996$). To visualize the overall halothane effects on HSQC chemical shifts, the normalized changes in the weighted average of the ^1H and ^{15}N chemical shifts with and without 2.2 mM halothane are color coded onto the protein structure (see below for structural determination), as shown in Fig. 1 *B*. Clearly, the most sensitive region is near W15. To further confirm that the concentration-dependent chemical shift changes are indeed a result of halothane binding instead of other nonspecific effects, a second, independent NMR method was used to measure the saturation transfer (26) between halothane and various residues. The percentage change in tr-HSQC peak intensity from the saturation transfer difference spectroscopy is mapped on the structure (Fig. 1 *C*), showing again the specific interaction between halothane and the protein near W15, A22, and A44. Neither chemical shift titration nor the saturation transfer difference spectroscopy showed significant halothane effects on M38, confirming the prediction from a computer simulation (27) and our own structural study (Part I (11)) that M38 is not directly involved in the halothane binding. Thus, the 3.5-fold enhancement in the halothane binding affinity due to L38M mutation must result from allosteric effects.

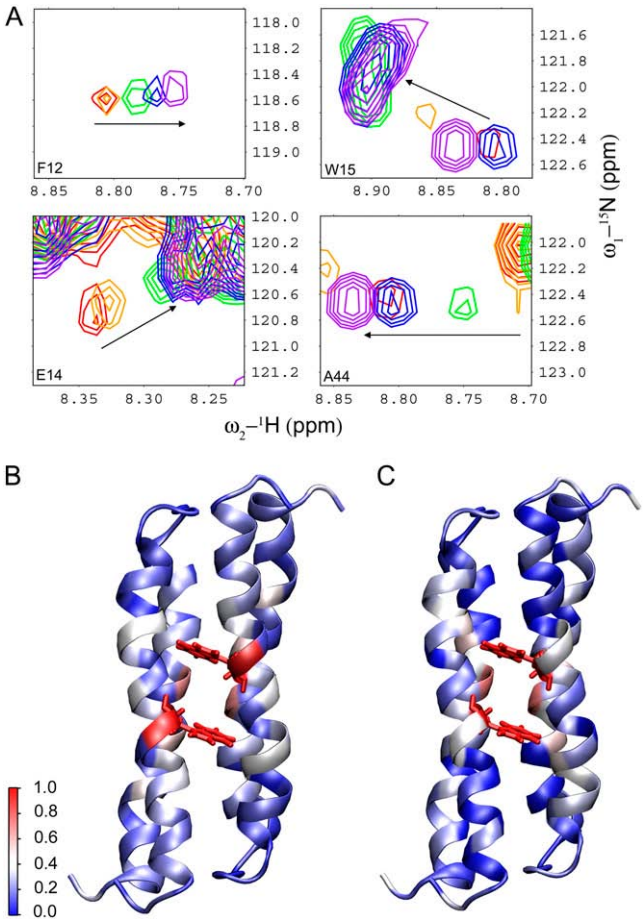

FIGURE 1 Halothane binding to the four-α-helix bundle $(A\alpha_2\text{-L1M/L38M})_2$. (*A*) Overlap of HSQC contour plots for residues F12, E14, W15, and A44 in response to halothane titration, which was done by adding neat halothane to the NMR sample in 0.3-μl increments. The same contour scale is used for all peaks in each plot to show relative intensities. The peak colors in the order of red, orange, green, blue, and purple indicate increasing concentrations of halothane from 0 to 2.2 mM. In the contours for W15 and A44, the shifted A44 peaks (*blue* and *purple*) overlap with the unshifted W15 peak (*red*). Notice that W15 shows a large chemical shift jump at the first titration point and greatly increased intensities at higher halothane concentrations. (*B*) Individual residues in the NMR-determined structure are color-coded according to their normalized chemical shift sensitivities to halothane titration, with blue to red representing the least to most sensitive, respectively. (*C*) Normalized saturation transfer NOE is mapped onto the NMR structure of $(A\alpha_2\text{-L1M/L38M})_2$ using the blue-white-red color code.

High-resolution structures with a bound halothane

Parallel to the studies without anesthetics as described in Part I (11)), the same batch of the expressed proteins was used in this study to determine the $(A\alpha_2\text{-L1M/L38M})_2$ structure in the presence of halothane. The same suite of heteronuclear, multidimensional NMR experiments was performed for assignment and structure determination. The NOE connectivity and chemical shift index (CSI) pattern resemble those shown in Fig. 3 of Part I (11)). Again, two helical segments, from R5 to E27 and from E36 to R58, are readily identifiable in the NOE connectivity and CSI. The two termini and the glycine linker between the two helices appear to be unstructured based on the CSI and dynamics results (see below). The statistics of the 20 structures with the lowest target function is given in Table 1. The overall backbone RMSD is 1.72 ± 0.39 Å; the backbone RMSD of the helical regions is 1.05 ± 0.28 Å. The insignificant difference in RMSD between the apo- and halothane-bound protein structures is likely due to the difference in the spectral quality and the different numbers of total constraints available for the structural calculation. In the presence of halothane, at least two intermolecular NOE peaks were positively identified in 2D NOESY between halothane and L18 and A44 (Fig. 2). Structural calculations with the inclusion of a halothane molecule clearly define the halothane binding pocket, which is shown to be bordered by the aromatic side chains of W15 and the hydrophobic side chains of L18 and A44 in the dimeric form (Fig. 3 *E*). Fig. 3, *A* and *B*, show the superposition of the structures with and without halothane in the monomer and dimer forms, respectively, exhibiting nearly the same secondary and tertiary monomer structures and pronounced quaternary structural changes after the addition of halothane. The side-chain arrangements surrounding the primary halothane binding site

TABLE 1 Structural statistics of 20 (Aα_2-L1M/L38M)$_2$ structures with halothane

NMR structure	Statistic
Restraints per monomer	
NOE distances	
Intraresidue	144
Short range (i-j = 1)	128
Medium range (1< i-j ≤ 4)	96
Long range (i-j > 4)	15
Dimer (intermonomer)	6
Dihedral angles	72
Hydrogen bonds	20
Residual upper limit constraints violations number > 0.5 Å	0
Residual dihedral angle constraints violations number > 5°	0
Backbone RMSD	
Residues 5-27, 36-58, 205-227, 236-258	1.05 ± 0.28 Å
All residues (1-62, 201-262)	1.72 ± 0.39 Å
Heavy atom RMSD	
Residues 5-27, 36-58, 206-226, 236-258	1.56 ± 0.32 Å
All residues (1-62, 201-262)	2.07 ± 0.36 Å
Ramachandran plot	
Residues in most favored regions	91.0%
Residues in allowed regions	8.9%
Residues in disallowed regions	0.2%

without and with a bound halothane are depicted in Fig. 3, *C* and *D*, respectively, and the packing details of halothane interaction with the protein at the binding site are shown in Fig. 3 *E*. Whereas the halothane orientation in the pocket is not fixed, there is a clear orientation preference in binding interaction in the bundle of structures (Fig. 4) because of cation-pi type of interaction between the partial positive charge on the hydrogen atom of halothane (28) and the aromatic ring of W15. Among the 20 lowest-energy structures, 12 have a halothane orientation as shown in Fig. 3 *E*, with halothane's Br and Cl each interacting with one of the two hydrophobic side chains of L18, and the hydrogen and the –CF_3 moiety orienting toward the W15 aromatic ring and the A44 side chain, respectively. In the remaining 8 structures, the halothane flips ~180° to point the proton to the aromatic ring of the other W15.

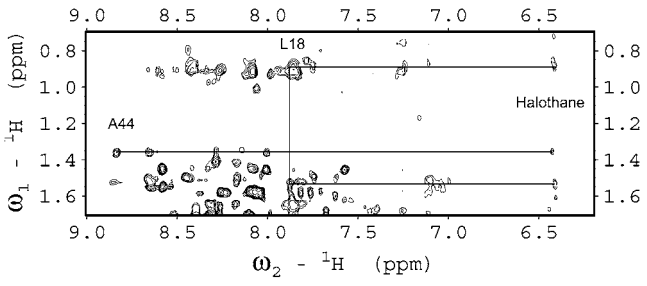

FIGURE 2 A contour plot of a ^{1}H-^{1}H 2D NOESY spectrum showing unambiguous crosspeaks between halothane resonance at ~6.4 ppm and the side chains of L18 and A44.

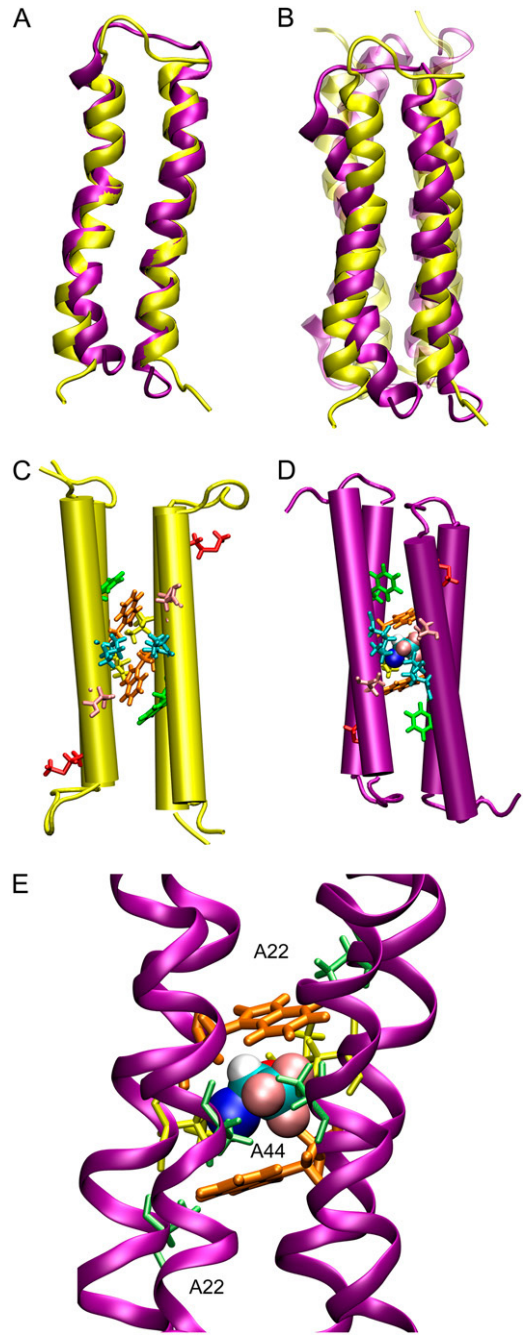

FIGURE 3 Comparison of high-resolution NMR structures of (Aα_2-L1M/L38M)$_2$ determined with and without halothane. (*A*) The monomer structure determined in the presence of halothane (purple) is superimposed onto the structure of the apoprotein (*yellow*). (*B*) Superposition of the dimer structures. Notice the quaternary structural changes and supercoiling of the helices in the presence of halothane. (*C*) Side view of hydrophobic core of the four-α-helix bundle in the absence of halothane. (*D*) Side view of hydrophobic core of the four-α-helix bundle with a halothane bound in the primary binding site. (*E*) Detailed interactions between halothane and the residues surrounding the anesthetic binding pocket. In *C*, *D*, and *E*, important side chains are shown in licorice representation: W15 (*orange*); K47 (*cyan*); E43 (*pink*); F12 (*green*); and A22 and A44 (*lime*). The halothane molecule is shown in VDW spheres: C (*cyan*); H (*white*); Cl (*blue*); Br (*red*); and F (*pink*).

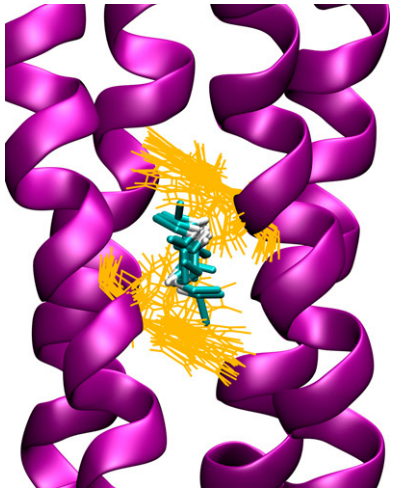

FIGURE 4 Orientations of halothane molecules in the binding pocket. A bundle of 20 halothane molecules (C-C bond (*cyan*); C-H bond (*white*) is depicted in relation to the bundle of W15 side chains (*orange*) in the 20 lowest energy structures. Although the halothane orientation is not fixed, the hydrogen, with partial positive charge, has the tendency to point to the aromatic ring of W15 due to cation-pi type of interaction.

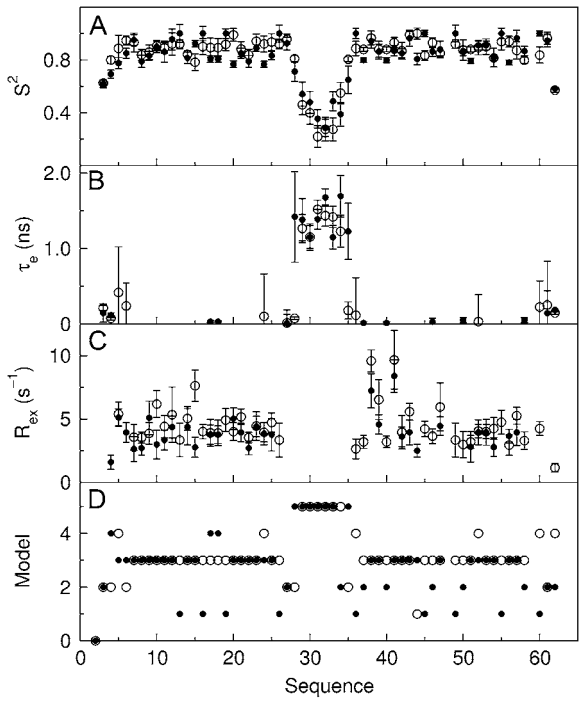

FIGURE 5 Comparison of ($A\alpha_2$-L1M/L38M)$_2$ dynamics in the presence and absence of halothane binding. (*A*) The squared order parameter (S^2), (*B*) the local correlation time (τ_e), (*C*) the exchange contribution (R_{ex}), and (*D*) model number used in the model-free analysis are plotted as a function of the residue numbers of the four-α-helix bundle, depicting the dynamics in the absence (○) and presence (●) of 2.2 mM of halothane. Notice that halothane stabilizes overall protein motion as evidenced by the increased S^2 in the immediate vicinity of W15 and the globally reduced R_{ex} terms at many residues.

Anesthetic effects on backbone dynamics

The backbone dynamics was determined by analyzing the R_1, R_2, and hetNOE of the backbone amide ^{15}N with and without halothane using the Modelfree approach (17,18). In addition, the conformation exchange on the μs-ms timescale was examined using the CPMG R_2 dispersion measurements. The effects of halothane binding on the local and global dynamics are depicted in Figs. 5 and 6. Fig. 5 shows the conventional Modelfree analysis, depicting the generalized order parameter, the correlation time of the fast local motion (τ_e), the exchange contribution to the relaxation (R_{ex}) (29), and the model number used to fit the data. As in the case without anesthetics, the two termini and the loop regions are significantly more flexible, with order parameters lower than 0.5. The loop region does not meet the basic Lipari-Szabo assumption and can only be fitted with Model 5. In the presence of halothane, the residues in the immediate vicinity of the binding site showed slightly elevated order parameters, becoming more ordered than without halothane. The most profound changes are seen in the global distribution of the R_{ex} term in the helical regions. Overall, R_{ex} is reduced upon halothane binding, suggesting a lesser degree of conformational exchange. The involvement of nonzero R_{ex} terms in many residues is confirmed by the R_2 dispersion measurements, which are independent of the model selection or the spectral density mapping. As shown in Fig. 6, many residues exhibit the R_2 dependence on the CPMG frequencies. The ΔR_2 values, which are estimated from the R_2 values at the two extreme CPMG frequencies achievable with our NMR hardware, display the same distribution pattern as R_{ex} along the protein sequence (Fig. 6 *B*). It should be noted that the ΔR_2 measured by the relaxation dispersion underlies the phenomenological nonzero R_{ex} term in the Modelfree analysis, albeit the two are not expected to be identical (25) because the two experimental methods are sensitive to motions on different timescales. Nevertheless, the overall trend is clear, and the binding of halothane reduces the conformational exchange on the global scale. The significance of this reduction in R_{ex} (or ΔR_2) will be discussed below. As in the case without halothane, two residues, M38 and C41, still show a larger R_{ex} than other residues, albeit halothane reduced the R_{ex} values by a factor of 2. Exchange parameters, R_{20}, Φ_{ex}/k_{ex}, and k_{ex}, determined for several residues using the fast exchange limit approximation (Eq. 4) to fit the R_2 dispersion data, are shown in Supplementary Material, Table S1. There seems to be also a slight tendency that halothane binding makes the loop region more ordered as shown in the S^2 values. This is supported by the slightly elevated R_2 values for some of the loop residues in the R_2 dispersion measurements (e.g., G30 in Fig. 6 *A*). However, since the R_2 dispersion method is prone to artifacts when R_2 is not significantly larger than R_1 (30), which is indeed the case for the loop residues, the small difference in the R_2 dispersion with and without halothane should be taken with caution for the loop and terminal residues. Using the same method as in Part

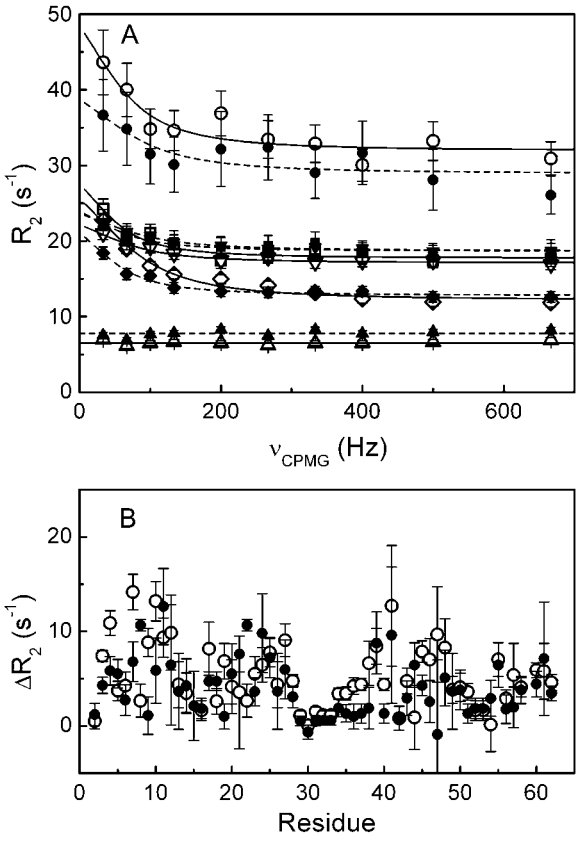

FIGURE 6 (*A*) Representative plots of the ^{15}N transverse relaxation rate, R_2, as a function of the CPMG field strength, ν_{CPMG}, for L4 (◇), G30 (Δ), M38 (□), C41 (○), and E50 (∇) in (Aα_2-L1M/L38M)$_2$ without (*open symbols*) and with (*solid symbols*) 2.2 mM halothane at 18.8 T (800 MHz). Uncertainties in R_2 were determined from the signal/noise ratio using Eq. 3. The $R_2(\nu_{CPMG})$ dispersion profiles for L4, M38, C41, and E50 demonstrate the contribution of conformation exchange to the ^{15}N transverse relaxation rate. The solid and dash lines are the best fit to the data for the protein in the absence and presence of the anesthetic, respectively, using Eq. 4. G30 shows no conformation exchange and is presented here as a reference. (*B*) Values of $\Delta R_2 = R_2(\nu_{CPMG}=33.3\text{Hz}) - R_2(\nu_{CPMG} = 666.7\text{Hz})$ are plotted as a function of residue numbers in (Aα_2-L1M/L38M)$_2$ without (○) and with (●) halothane at 18.8 T. Most residues show a decreased ΔR_2 in the presence of halothane, indicating that halothane suppresses the global conformational exchange in the protein.

I (11) to search for the best-fitted τ_m value, the Modelfree calculations yielded the global tumbling time of 5.00 ± 0.08 ns, in agreement with the global tumbling time of the apo protein.

DISCUSSION

Primary anesthetic binding site in the four-α-helix bundle

Four-α-helix bundle is a common scaffold found in many important functional proteins. For example, the transmembrane domains of anesthetic-sensitive superfamily of Cys-loop receptors are composed of pseudosymmetric pentamers of four-α-helix bundles. Serving as a model for anesthetic protein targets, (Aα_2-L1M/L38M)$_2$ was designed with a few iterations of design changes aimed at improving the binding affinity for volatile anesthetics (8,9). Our structural studies of (Aα_2-L1M/L38M)$_2$ in the absence of a bound anesthetic, as detailed in Part I (11) suggested a primary binding site between the two W15 side chains in a dimer and an amphipathic lateral access pathway from the aqueous phase through the flexible C-terminal helix interface into this binding site. These findings are somewhat unexpected because the intended binding sites by design are closer to the two ends of the hydrophobic core of the four-helix bundle, and thus there should be two sites that are mirror images of each other. In the present structural study with halothane, we confirmed that the main halothane binding site is indeed sandwiched between the two W15 residues. The chemical shift changes in response to titration with varying concentrations of halothane, the saturation transfer experiment, and 2D NOESY experiment all indicate that the preferred halothane interaction site are in the middle section of the four-helix bundle, instead of between W15 and M38 as the latest iteration of design had intended. The apparent dissociation constant for halothane binding to (Aα_2-L1M/L38M)$_2$ is estimated to be in the submillimolar range based on the fluorescence quenching on (Aα_2-L38M)$_2$ (9). Our chemical shift titration experiments, which measure the halothane influence on the protein backbone amide nitrogen and proton chemical shifts, probe the relative involvement of individual residues in the anesthetic binding. Since the side chains at the binding site are more directly involved in the interaction than the backbone, the site-specific K_d determined from the backbone chemical shifts does not necessarily reflect the true binding affinity at the interaction site. Nevertheless, the approximate K_d value obtained from the chemical shift titration measurements is consistent with the apparent K_d from the fluorescence quenching experiments (9).

It is interesting to note that when the experimental structures were used in a docking search for potential halothane binding sites, we found that the site between two W15 side chains is highly preferred (~98%) but not exclusive in the apoprotein. In contrast, with the lowest energy structure determined in the presence of halothane, Autodock (31) found the halothane binding site to be exclusively between W15 side chains. The estimated free energy of binding from Autodock is –3.35 kcal/mol (4.89 mM), which is in agreement with the experimental titration data.

An induced fit for anesthetic binding

Detailed structural analysis revealed that the monomeric helix-turn-helix fold is very similar in the two structural bundles with and without a bound anesthetic, as shown in Fig. 3 *A*. When fitting the helical regions of the monomers, the RMSD between the two structural bundles is ~1.5 Å, which is only slightly larger than the RMSD of the monomers

among the 20 lowest-energy structures of each bundle. Thus, halothane binding did not greatly affect the monomer (secondary and tertiary) structure. As shown in Fig. 3 *B*, the most significant structural change upon halothane binding is the quaternary association of the four helices in the dimer. There is a vertical shift of the monomers relative to each other by approximately half a helix turn and a super-coil twisting of the helices when a halothane molecule is bound at the site between the two W15s. These quaternary structural changes removed the asymmetry found in the apoprotein due to wider separation between helix 2 and helix 2′. The halothane-induced quaternary changes led to a better fitting between halothane and the amphipathic cavity of the binding site. Measured by the Q-SiteFinder program (32), the binding cavity bordered primarily by the side chains of W15, L18, and A44 (Fig. 3, *D* and *E*) reduces its size from ~381 Å^3 in the structures without halothane to ~162 Å^3 in the structures determined with halothane (after removing halothane from the structure). The latter value better matches the molecular volume of halothane (~130 Å^3 (33,34)). Thus, our structural data suggest an induced fit between halothane and its binding site. The high structural flexibility of the apoprotein, the lateral opening between helix 2 and helix 2′ for direct access to the binding site from the aqueous phase, and the quaternary structural re-arrangement for an induced fit can all contribute to an increase in the binding on-rate. As evidenced in the packing between the halothane molecule and the residues surrounding the binding pocket (Fig. 3 *E*), the interaction at the binding site is both hydrophobic and electrostatic in nature. Optimization of the fitting in the binding site and the closure of the lateral pathway as a result of the twisting of helices 2 and 2′ relative to helices 1 and 1′ will likely decrease the binding off-rate, thereby achieving the high-affinity specific binding of halothane in this designed protein.

Implications of anesthetic effects on local and global dynamics

In addition to the structural changes, halothane binding to the four-α-helix bundle also resulted in profound changes in the protein dynamics, not only locally but also globally at residues remote from the binding site. This finding is important because protein function always involves protein motion. Thus, the four-α-helix bundle offers more than just a structural model. The characteristics of halothane effects on the dynamics of (Aα_2-L1M/L38M)$_2$ may have universal implications on how anesthetic binding to protein ultimately leads to changes in protein functions (1–3,7,35–37).

In the absence of halothane, (Aα_2-L1M/L38M)$_2$ appears extremely dynamic on the NMR timescale (11). Model-free analysis showed that many residues in the helical regions contain the R_{ex} contribution to the backbone amide ^{15}N relaxation, suggesting the presence of a conformational exchange process at these residues (18,28,38). This finding is confirmed in this study by the R_2 dispersion measurements. By comparing the model-free analyses of the relaxation data with and without halothane as shown in Fig. 5 and of the R_2 dispersion data as shown in Fig. 6, it is clear that halothane binding not only stabilizes the residues in direct contact with halothane, but also reduces the R_{ex} (or ΔR_2) on a global scale. The most noticeable R_{ex} changes in (Aα_2-L1M/L38M)$_2$ are at W15 and near M38 and C41. In the apoprotein, W15 signal is relatively weak (hence precluding the R_2 dispersion measurement), presumably due to an intermediate exchange. Indeed, when the site is not occupied, there is a large degree of orientation freedom for the W15 side chains within the hydrophobic core. The NMR structure of the apoprotein suggests that W15 side chains tend to swing toward F12 to form an aromatic ring stack within the long stretch of hydrophobic core, leaving a large space between the W15 side chains to accept halothane. When the site is occupied, the two W15 side chains are locked into a parallel configuration (Fig. 3, *D* and *E*) with reduced local flexibility, as indicated by the increased order parameter at W15 and nearby residues. This not only changes the chemical shift but also increases the intensity of W15 in HSQC (Fig. 1 *A*). One of the direct consequences of the reduced W15 side chain flexibility—in addition to the induced fitting for high-affinity halothane binding as discussed above—is the largest decrease of the R_{ex} term associated with W15 (Fig. 3 *E*).

As discussed in Part I (11), another dynamic hotspot in (Aα_2-L1M/L38M)$_2$ is located near M38 and C41. Both of these residues showed a large R_{ex} term compared to the rest of the protein when no halothane is bound. It is known that a point mutation at residue 38 from Leu to Met can result in a 3.5-fold increase in halothane binding. Such an increase could be due to changes in either structure or dynamics, or both. Structurally, Leu-Met mutation has been shown to be well tolerated by numerous studies. Because M38 (or L38) is not even part of the halothane binding site according to the NMR structure, local steric effects in a structural sense are unlikely to be the cause of the increased binding affinity after the mutation. In searching for other possible explanations, we believe that global dynamics is an obvious candidate, given the unusual dynamics property near the mutation site. The allosteric coupling between W15 and M38 is clearly evident in the large reduction of the R_{ex} term at M38 and C41 on halothane binding at W15. This suggests that residue 38 is situated at a pivotal point to control the global dynamics of the protein. Although Leu and Met are close on the hydrophobicity scale (39), methionine's side chain is longer and narrower than leucine's side chain. Residue 38 is at the first heptad *g* position in the first turn of helix 2 after the flexible glycine linker. From the apoprotein structure, it can be seen clearly that the M38 side chain is sandwiched between the adjacent L37 and the more distant E27 and A23, all of which congregate at the two ends of the flexible glycine loop. The long and linear M38 side chain can either point toward the glycine loop or toward the lateral aqueous phase, depending on the glycine loop orientation. If L38 resumes the same local

structure as M38, its side chain has predictably less orientation freedom relative to the glycine loop due to its bulkier branching methyl groups. Therefore, it is conceivable that the mobility at residue 38 in relation to the flexible linker is critical to the opening and closing of the lateral pathway between helix 2 and helix 2′. The higher halothane binding affinity found in the L38M mutation can be explained by the increased on-rate, whereas the off-rate should be dictated by the W15 ring stacking and induced fit after halothane has occupied the binding site, which would be similar irrespective of L38 or M38.

In support of this viewpoint is the dynamics change at E43 and K47, where sizeable R_{ex} terms can be seen when halothane is absent. After halothane binding, the high-resolution NMR structures reveal that the quaternary structural changes shift E43 of one monomer to almost the same level as K47 of the other monomer. The super-coil twisting brings E43 at heptad *b* position closer to K47 at heptad *e* position of the opposing helix. The electrostatic interaction stabilizes E43 and closes the interface (and thus the lateral access pathway) between helices 2 and 2′. As a consequence, both E43 and K47 show a significantly reduced R_{ex} term after halothane binding.

Our results suggest an interesting interplay between structural fitting and dynamical contribution to anesthetic binding at protein targets. From a pure structural viewpoint without considering protein mobility, the space between two W15 side chains in the apoprotein would not seem ideal for halothane binding. As discussed above, there is a large discrepancy between the cavity size (381 $Å^3$) and the volume of the anesthetic molecule (130 $Å^3$) for a snug structural fit. However, the opening between helices 2 and 2′ and their conformational flexibility create an easy access directly from the aqueous phase to this site. The intrinsic global mobility of this dimeric protein and the interaction-induced structural fitting between halothane and the key residues at the binding site make this site more favorable than other potential sites. For example, the minor sites found by the Autodock program in the apoprotein between F12 and F52 would be theoretically suitable for halothane binding. These minor sites, however, are not occupied with high affinity due to divergence of the structural and dynamical factors at these sites. As discussed in Part I (11), the side chain of F52 seems to be ''out of place'' in the aqueous phase. Although the local rotational freedom of F12 and F52 side chains would allow halothane to bind, the absence of a consequent structural change to secure the binding would render any halothane occupancy between F12 and F52 short-lived. Similarly, Q-SiteFinder revealed two amphipathic pockets bordered mainly by A8, F12, L51, L54, and R58 of one monomer and L26, E27, L37, M38, and C41 of the other monomer, along with three residues from the glycine loop. These pockets have a volume of 303 $Å^3$ but show no interaction with halothane experimentally and yield no population by flexible docking. The controlling factor in this later case is likely to be the protein dynamics. Thus, when searching for important anesthetic interaction site or sites in neuronal proteins to understand the molecular mechanisms of general anesthesia, one must analyze and differentiate the structural and dynamical contributions to the functional consequences of anesthetic-protein interactions.

In conclusion, we identified a novel anesthetic binding site in the designed four-α-helix bundle $(A\alpha_2\text{-L1M/L38M})_2$ by solving its high-resolution structure in the presence of halothane. Different from the designed locations, this site becomes preferred over other potential sites, including the two designed sites, for anesthetic binding after the interaction between the anesthetic and protein has occurred. The intrinsic global dynamics characteristics of this protein make the induced fitting possible, and the induced structural fitting upon anesthetic binding, in turn, modifies the local and global dynamics of the protein. For neuronal proteins, the latter aspect is likely to account for functional change of the proteins, ultimately leading to the anesthetizing effects. It should be pointed out also that we proposed more than a decade ago, based on the analysis of xenon (6), that some molecules would not normally be classified as general anesthetics due to their lack of basic properties found in common anesthetizing agents, but they nevertheless can produce anesthesia by gaining these properties after interactions with their targets takes place (e.g., induced dipole in xenon). We now show an example of a related phenomenon, namely, that the protein targets can be turned into relevant to anesthetic action only after the interaction between anesthetic and protein has taken place. The value of the designed four-α-helix bundle as a model for anesthetic targets lies not only in its structural resemblance to the ubiquitous scaffold found in many functional proteins, but also in its dynamics characteristics that are perhaps more relevant to the functional response to anesthetics (1,2).

SUPPLEMENTARY MATERIAL

To view all of the supplemental files associated with this article, visit www.biophysj.org.

The authors thank Professor Rieko Ishima for her valuable suggestions and stimulating discussions on R2 relaxation dispersion studies.

This work was supported in part by grants from the National Institutes of Health (R37GM049202 to Y.X. and P.T., R01GM056257 to PT, and P01GM055876 to Y.X. and J.S.J.).

REFERENCES

1. Szarecka, A., Y. Xu, and P. Tang. 2007. Dynamics of firefly luciferase inhibition by general anesthetics: Gaussian and anisotropic network analyses. *Biophys. J.* 93:1895–1905.
2. Tang, P., and Y. Xu. 2002. Large-scale molecular dynamics simulations of general anesthetic effects on the ion channel in the fully hydrated membrane: the implication of molecular mechanisms of general anesthesia. *Proc. Natl. Acad. Sci. USA.* 99:16035–16040.

3. Yonkunas, M. J., Y. Xu, and P. Tang. 2005. Anesthetic interaction with ketosteroid isomerase: insights from molecular dynamics simulations. *Biophys. J.* 89:2350–2356.
4. Campagna, J. A., K. W. Miller, and S. A. Forman. 2003. Mechanisms of actions of inhaled anesthetics. *N. Engl. J. Med.* 348:2110–2124.
5. Eckenhoff, R. G., and J. S. Johansson. 1997. Molecular interactions between inhaled anesthetics and proteins. *Pharmacol. Rev.* 49:343–367.
6. Xu, Y., and P. Tang. 1997. Amphiphilic sites for general anesthetic action? Evidence from 129Xe-[1H] intermolecular nuclear Overhauser effects. *Biochim. Biophys. Acta.* 1323:154–162.
7. Xu, Y., P. Tang, and S. Liachenko. 1998. Unifying characteristics of sites of anesthetic action revealed by combined use of anesthetics and non-anesthetics. *Toxicol. Lett.* 100–101:347–352.
8. Johansson, J. S., B. R. Gibney, F. Rabanal, K. S. Reddy, and P. L. Dutton. 1998. A designed cavity in the hydrophobic core of a four-α-helix bundle improves volatile anesthetic binding affinity. *Biochemistry.* 37:1421–1429.
9. Johansson, J. S., D. Scharf, L. A. Davies, K. S. Reddy, and R. G. Eckenhoff. 2000. A designed four-α-helix bundle that binds the volatile general anesthetic halothane with high affinity. *Biophys. J.* 78: 982–993.
10. Pidikiti, R., M. Shamim, K. M. Mallela, K. S. Reddy, and J. S. Johansson. 2005. Expression and characterization of a four-α-helix bundle protein that binds the volatile general anesthetic halothane. *Biomacromolecules.* 6:1516–1523.
11. Ma, D., N. R. Brandon, T. Cui, V. Bondarenko, C. Canlas, J. S. Johansson, P. Tang, and Y. Xu. 2008. Four-α-helix bundle with designed anesthetic binding pockets. Part I: Structural and dynamical analyses. *Biophys. J.* 94:4454–4463.
12. Guntert, P., C. Mumenthaler, and K. Wuthrich. 1997. Torsion angle dynamics for NMR structure calculation with the new program DYANA. *J. Mol. Biol.* 273:283–298.
13. Xu, Y., P. Tang, L. Firestone, and T. T. Zhang. 1996. 19F nuclear magnetic resonance investigation of stereoselective binding of isoflurane to bovine serum albumin. *Biophys. J.* 70:532–538.
14. Xu, Y., T. Seto, P. Tang, and L. Firestone. 2000. NMR study of volatile anesthetic binding to nicotinic acetylcholine receptors. *Biophys. J.* 78:746–751.
15. Fielding, L. 2003. NMR methods for the determination of protein-ligand dissociation constants. *Curr. Top. Med. Chem.* 3:39–53.
16. Morton, C. J., D. J. Pugh, E. L. Brown, J. D. Kahmann, D. A. Renzoni, and I. D. Campbell. 1996. Solution structure and peptide binding of the SH3 domain from human Fyn. *Structure.* 4:705–714.
17. Lipari, G., and A. Szabo. 1982. Model-free approach to the interpretation of nuclear magnetic resonance relaxation in macromolecules. 1. Theory and range of validity. *J. Am. Chem. Soc.* 104:4546–4559.
18. Lipari, G., and A. Szabo. 1982. Model-Free Approach to the Interpretation of Nuclear Magnetic Resonance Relaxation in Macromolecules. 2. Analysis of Experimental Results. *J. Am. Chem. Soc.* 104:4559–4570.
19. Mandel, A. M., M. Akke, and A. G. Palmer III. 1995. Backbone dynamics of *Escherichia coli* ribonuclease HI: correlations with structure and function in an active enzyme. *J. Mol. Biol.* 246:144–163.
20. Loria, J. P., M. Rance, and A. G. Palmer. 1999. A Relaxation-Compensated Carr-Purcell-Meiboom-Gill Sequence for Characterizing Chemical Exchange by NMR Spectroscopy. *J. Am. Chem. Soc.* 121:2331–2332.
21. Tollinger, M., N. R. Skrynnikov, F. A. Mulder, J. D. Forman-Kay, and L. E. Kay. 2001. Slow dynamics in folded and unfolded states of an SH3 domain. *J. Am. Chem. Soc.* 123:11341–11352.
22. Wishart, D. S., C. G. Bigam, J. Yao, F. Abildgaard, H. J. Dyson, E. Oldfield, J. L. Markley, and B. D. Sykes. 1995. 1H, 13C and 15N chemical shift referencing in biomolecular NMR. *J. Biomol. NMR.* 6:135–140.
23. Mulder, F. A., N. R. Skrynnikov, B. Hon, F. W. Dahlquist, and L. E. Kay. 2001. Measurement of slow (micros-ms) time scale dynamics in protein side chains by (15)N relaxation dispersion NMR spectroscopy: application to Asn and Gln residues in a cavity mutant of T4 lysozyme. *J. Am. Chem. Soc.* 123:967–975.
24. Luz, Z., and S. Meiboom. 1963. Nuclear magnetic resonance study of the protolysis of trimethylammonium ion in aqueous solution—order of the reaction with respect to solvent. *J. Chem. Phys.* 39:366–370.
25. Perazzolo, C., M. Verde, S. W. Homans, and G. Bodenhausen. 2007. Evidence of chemical exchange in recombinant major urinary protein and quenching thereof upon pheromone binding. *J. Biomol. NMR.* 38:3–9.
26. Meyer, B., and T. Peters. 2003. NMR spectroscopy techniques for screening and identifying ligand binding to protein receptors. *Angewandte Chemie International ed.* 42:864–890.
27. Davies, L. A., Q. Zhong, M. L. Klein, and D. Scharf. 2000. Molecular dynamics simulation of four-α-helix bundles that bind the anesthetic halothane. *FEBS Lett.* 478:61–66.
28. Tang, P., I. Zubryzcki, and Y. Xu. 2001. Ab initio calculation of structures and properties of halogenated general anesthetics: halothane and sevoflurane. *J. Comput. Chem.* 22:436–444.
29. Kneller, J. M., M. Lu, and C. Bracken. 2002. An effective method for the discrimination of motional anisotropy and chemical exchange. *J. Am. Chem. Soc.* 124:1852–1853.
30. Ishima, R., and D. A. Torchia. 2003. Extending the range of amide proton relaxation dispersion experiments in proteins using a constant-time relaxation-compensated CPMG approach. *J. Biomol. NMR.* 25:243–248.
31. Morris, G. M., D. S. Goodsell, R. S. Halliday, R. Huey, W. E. Hart, R. K. Belew, and A. J. Olson. 1998. Automated docking using a Lamarckian genetic algorithm and an empirical binding free energy function. *J. Comput. Chem.* 19:1639–1662.
32. Laurie, A. T., and R. M. Jackson. 2005. Q-SiteFinder: an energy-based method for the prediction of protein-ligand binding sites. *Bioinformatics.* 21:1908–1916.
33. Lopez, M. M., and D. Kosk-Kosicka. 1997. Entropy-driven interactions of anesthetics with membrane proteins. *Biochemistry.* 36:8864–8872.
34. Eckenhoff, M. F., K. Chan, and R. G. Eckenhoff. 2002. Multiple specific binding targets for inhaled anesthetics in the mammalian brain. *J. Pharmacol. Exp. Ther.* 300:172–179.
35. Liu, Z., Y. Xu, and P. Tang. 2005. Molecular dynamics simulations of C2F6 effects on gramicidin A: implications of the mechanisms of general anesthesia. *Biophys. J.* 88:3784–3791.
36. Liu, Z., Y. Xu, and P. Tang. 2006. Steered molecular dynamics simulations of Na+ permeation across the gramicidin A channel. *J. Phys. Chem.* 110:12789–12795.
37. Szarecka, A., Y. Xu, and P. Tang. 2007. Dynamics of heteropentameric nicotinic acetylcholine receptor: implications of the gating mechanism. *Proteins.* 68:948–960.
38. Krizova, H., L. Zidek, M. J. Stone, M. V. Novotny, and V. Sklenar. 2004. Temperature-dependent spectral density analysis applied to monitoring backbone dynamics of major urinary protein-I complexed with the pheromone 2- sec-butyl-4,5-dihydrothiazole. *J. Biomol. NMR.* 28:369–384.
39. Kyte, J., and R. F. Doolittle. 1982. A simple method for displaying the hydropathic character of a protein. *J. Mol. Biol.* 157:105–132.